# Design and Experimental Verification of a Transimpedance Amplifier for 64-Gb/s PAM-4 Optical Links

Bart Moeneclaey, *Member, IEEE*, Jochen Verbrugghe, Joris Lambrecht, Elad Mentovich,
Paraskevas Bakopoulos, *Member, IEEE*, Johan Bauwelinck, *Member, IEEE*, and Xin Yin, *Member, IEEE*

*(Top-Scored Paper)*

***Abstract*—The use of four-level pulse-amplitude modulation (PAM-4) has emerged as a solution to increase the serial rate in short-range optical links, offering twice the data throughput but requiring similar bandwidth as on–off keying. However, the receiver design should take into account the increased susceptibility of PAM-4 to noise, intersymbol interference, and nonlinearity. This papers explores these challenges, and details the design of a transimpedance amplifier (TIA) for 64-Gb/s PAM-4 optical links. The TIA was implemented in 0.13-μm SiGe BiCMOS, and has a power consumption of 180 mW. It contains a digital gain controller, which allows switching between four gain modes, to tradeoff sensitivity against linearity. Bit error rate (BER) measurements show that the dynamic range is significantly extended: Optical modulation amplitudes between − 7 dBm and at least − 0.2 dBm yield a BER lower than $10^{-3}$.**

***Index Terms*—BiCMOS integrated circuits, optical receivers, optical fiber communication, pulse amplitude modulation.**

## I. INTRODUCTION

THE increasing popularity of multimedia applications such as high definition TV, video on demand, and cloud computing drives an explosive growth in bandwidth requirements in datacenters. In order to meet these requirements, the IEEE has set up a task force aiming to define a 400 Gb/s Ethernet specification. One of the solutions proposed by this task force entails 8 wavelength-multiplexed streams of 50 Gb/s PAM-4 signals over single-mode fiber [1]. By migrating from on-off keying (OOK), which is the traditional modulation format for these applications, to PAM-4, twice the data throughput can be achieved for a similar bandwidth.

This proposal has spurred research on various aspects of PAM-4 optical links supporting a similar serial data rate. The feasibility of using low-cost modulators or directly modulated lasers in such a scenario was experimentally demonstrated in [2]–[4]. PAM-4 drivers were presented in [5], [6], capable of 56 Gb/s and 40 Gb/s transmission, respectively. Furthermore, recently developed integrated circuits, performing forward error correction (FEC), feed-forward equalization (FFE) and decision-feedback equalization (DFE), allow complex real-time link experiments [7]–[10].

The use of PAM-4 presents several new challenges to the design of the receiver, in particular the TIA. More specifically, PAM-4 is more susceptible to noise, ISI, and receiver nonlinearities. Nevertheless, only few publications detail the design [11], [12] and experimental verification [13], [14] of a TIA in this context.

In [15], we reported on a TIA for 64 Gb/s PAM-4 optical links. The TIA was manufactured in 0.13 μm BiCMOS and, by switching between four gain modes, allows an increased dynamic range. The present paper is an invited extension of our work presented [15]. In Section II, we investigate in more detail the challenges associated with the use of PAM-4, and quantify the related penalties. Subsequently, Section III explores the design of the TIA in great depth, and discusses how the aforementioned challenges were addressed. The experimental setup and results are presented in Sections IV, and V, respectively. Section VI is devoted to the conclusions.

## II. PAM-4 CHALLENGES

This section explores the three aforementioned challenges w.r.t. the design of the TIA resulting from the use of PAM-4, and quantifies the associated penalties.

Let us initially assume that the system, comprised of the transmitter, channel, photodiode, and TIA, is linear. The output voltage $v(t)$ of the TIA is sampled at the symbol rate $1/T$,

Manuscript received August 2, 2017; revised October 18, 2017; accepted November 10, 2017. Date of publication November 14, 2017; date of current version February 24, 2018. This work was supported in part by the European Commision through the FP7 project MIRAGE (Contr. No. 318228), in part by H2020 project WIPE (Contr. No. 688572), and in part by the Institute for the Promotion of Innovation by Science and Technology in Flanders (IWT). *(Corresponding author: Bart Moeneclaey.)*

B. Moeneclaey, J. Lambrecht, J. Bauwelinck, and X. Yin are with the Department of Information Technology, IDLab, Ghent University—IMEC, Ghent 9052, Belgium (e-mail: bart.moeneclaey@ugent.be; joris.lambrecht@ugent.be; johan.bauwelinck@ugent.be; xin.yin@intec.ugent.be).

J. Verbrugghe was with the Department of Information Technology, IDLab, Ghent University—IMEC, Ghent 9052, Belgium. He is now with Broadcom Ltd., San Jose, CA 95131 USA (e-mail: jochen.verbrugghe@broadcom.com).

E. Mentovich is with the Mellanox Technologies, Yokneam 2069200, Israel (e-mail: mentovich@mellanox.com).

P. Bakopoulos is with the School of Electrical and Computer Engineering, National Technical University of Athens, Athens 15780, Greece (e-mail: pbakop@mail.ntua.gr).

Color versions of one or more of the figures in this paper are available online at http://ieeexplore.ieee.org.

Digital Object Identifier 10.1109/JLT.2017.2774005

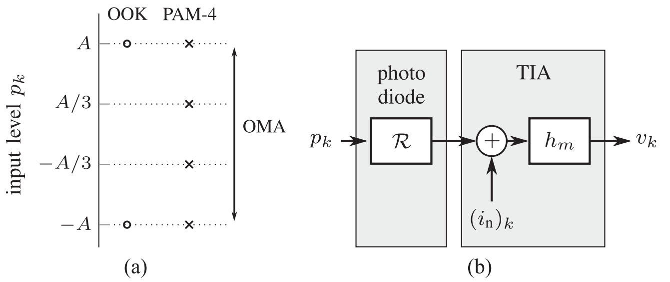

Fig. 1. OOK and PAM-4 input levels (a) and equivalent discrete-time linear receiver model (b).

resulting in $v_k = v(kT + \epsilon)$, to be used for symbol-by-symbol detection. Furthermore, we will assume that only the TIA introduces significant bandwidth effects and noise, such that the signal levels $p_k$ of the optical power incident to the photodiode are simply proportional to the transmitted symbols:

$$p_k \in \begin{cases} \{-A, A\} & \text{OOK} \quad (1a) \\ \{-A, -A/3, A/3, A\} & \text{PAM-4} \quad (1b) \end{cases}$$

As illustrated in Fig. 1(a), the OOK and PAM-4 constellations yield the same maximum magnitude $A$; the corresponding power swing or OMA equals 2A. Note that the actual incident power values corresponding to the input levels $p_k$ must be positive; they are obtained by adding to $p_k$ a suitable dc power which, however, does not impact the subsequent discussion. We will consider PAM-4 with Gray mapping, i.e., the bit labels corresponding to adjacent symbol levels differ in only one bit [16]. As shown in Fig. 1(b), the receiver is characterized by a photo diode with responsivity $\mathcal{R}$ and TIA with transimpedance impulse response $(\dots, h_{-1}, h_0, h_1, \dots)$ and input-referred white noise $(i_\text{n})_k$ with rms value $i_\text{n}^\text{rms}$. The output voltage sample $v_k$ can be expressed as

$$v_k = \underbrace{\mathcal{R} \cdot p_k \cdot h_0}_{\text{useful}} + \underbrace{\mathcal{R} \sum_{m \neq k} p_m \cdot h_{k-m}}_{\text{ISI}} + \underbrace{(v_\text{n})_k}_{\text{noise}} \tag{2}$$

where $(v_\text{n})_k$ is the noise at the TIA output, with rms value $v_\text{n}^\text{rms} = h_0 \cdot \eta \cdot i_\text{n}^\text{rms}$ and $\eta = \sqrt{\sum_m h_m^2 / h_0^2}$. (2) discerns the useful, ISI, and noise terms contributing to $v_k$. Note that $\eta \geq 1$, where equality holds when ISI is absent.

### A. *Level Spacing and ISI Penalty*

The effect of ISI and the reduced level spacing of PAM-4 on the BER is quantified using (1) and (2). First, let $\kappa = \sum_{m \neq 0} |h_m / h_0|$ denote the relative peak ISI magnitude. From (1) it follows that, regardless of modulation format, $|p_k| \leq A = \text{OMA}/2$, such that the worst-case ISI contribution in (2) equals $\pm\Delta/2$, with $\Delta = \mathcal{R} \cdot \text{OMA} \cdot h_0 \cdot \kappa$. Fig. 2 illustrates the resulting eye diagram for both OOK and PAM-4 modulation formats. At the decision instant, ISI bands are observed with height $\Delta$ for both modulation formats, reducing the vertical eye opening $d$, which equals

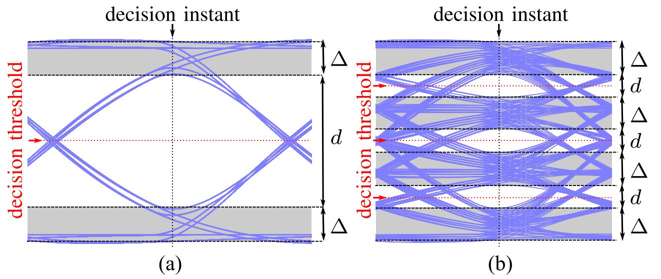

Fig. 2. Illustrative eye diagrams for (a) OOK and (b) PAM-4 with decision instant and decision threshold(s), as well as vertical eye opening(s) $d$ and ISI band height(s) $\Delta$ annotated.

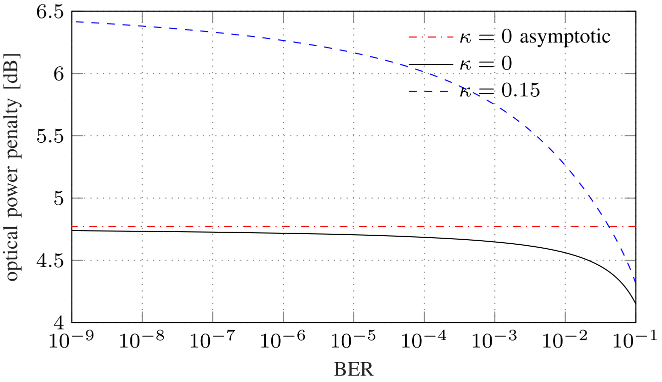

Fig. 3. Optical power penalty of PAM-4 compared to OOK without ISI ($\kappa = 0$) and with ISI ($\kappa = 0.15$).

$$d = \begin{cases} \mathcal{R} \cdot \text{OMA} \cdot h_0 \cdot (1 - \kappa) & \text{OOK} \quad (3a) \\ \frac{\mathcal{R} \cdot \text{OMA}}{3} \cdot h_0 \cdot (1 - 3\kappa) & \text{PAM-4} \quad (3b) \end{cases}$$

Note that, in the absence of ISI ($\kappa = 0$), the PAM-4 vertical eye opening (3b) is only one third of the OOK opening (3a). Furthermore, in the presence of ISI, the relative eye height reduction due to ISI is three times as large for PAM-4 as for OOK.

The effect of ISI on the BER can be approximated by assuming that the ISI term from (2) is uniformly distributed between $\pm\Delta/2$. Taking the decision thresholds at the midpoint(s) of the eye opening(s), it can be verified that the resulting BER equals

$$\text{BER} = \begin{cases} \frac{1}{2\kappa} \int_{-\kappa}^{\kappa} Q\left(\frac{\mathcal{R} \cdot \text{OMA} \cdot (1 + \epsilon)}{2\eta \cdot i_n^\text{rms}}\right) \text{d}\epsilon & \text{OOK} \quad (4a) \\ \frac{1}{2\kappa} \int_{-\kappa}^{\kappa} \frac{3}{4} Q\left(\frac{\mathcal{R} \cdot \text{OMA} \cdot (1 + 3\epsilon)}{6\eta \cdot i_n^\text{rms}}\right) \text{d}\epsilon & \text{PAM-4} \quad (4b) \end{cases}$$

Fig. 3 shows the optical power penalty of PAM-4 compared to OOK as a function of the operating BER, for the cases without and with ISI. In the absence of ISI ($\kappa = 0$), (4) reduces to the familiar BER expressions from [16], which show an optical power penalty of about 4.8 dB when comparing PAM-4 to OOK at very low BER; this reflects the ratio of their respective eye openings. This asymptotic penalty is also indicated in Fig. 3. In the presence of ISI, the penalty is considerably larger.

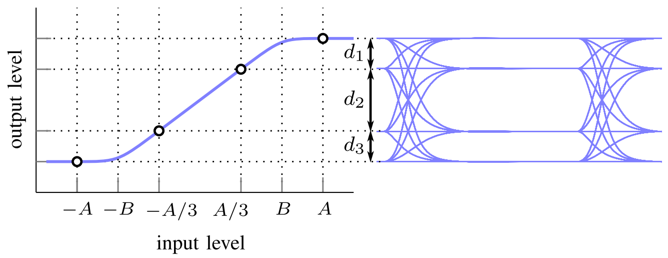

(a) (b)

Fig. 4. Illustrative nonlinear TIA input-output characteristic (a) and resulting eye diagram (b).

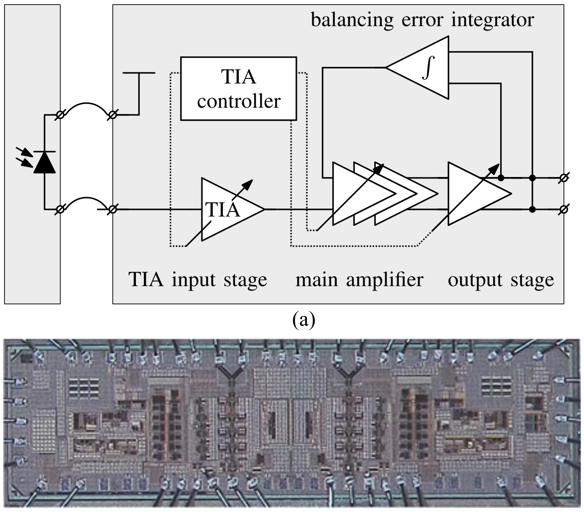

(a)

(b)

Fig. 5. TIA block diagram and die micrograph. (a) block diagram (b) die micrograph.

### B. Nonlinearity Penalty

With increasing input power, our previous assumption of linearity becomes less valid. Fig. 4(a) shows a typical receiver nonlinear input-output characteristic, which saturates for input amplitudes exceeding $B$. Consider the signal levels at the input of the receiver from (1b) and assume that $A/3 < B < A$, as shown in Fig. 4(a). The resulting output eye diagram (ignoring ISI) is displayed in Fig. 4(b). Because of the nonlinear characteristic, the vertical outer eye openings $d_1$ and $d_3$ are smaller than the vertical inner eye opening $d_2$. Further increasing $A$ would reduce the outer eye opening and, therefore, deteriorate the associated BER. This contrasts the linear behavior where the BER improves with increasing input level, as follows from (4b).

Assuming the maximum output swing is fixed, the input-referred linear range $(-B, B)$ is inversely proportional to the receiver gain. Hence, the nonlinearity penalty can be avoided for a large range of OMAs by appropriately adjusting the receiver gain, such that the output swing is kept at a reasonable level within the linear region.

## III. Transimpedance Amplifier Architecture

Fig. 5(a) shows a simplified block diagram of the TIA, which was based on the circuit presented in [13], [17]. The datapath consists of a single-ended TIA input stage, followed by a differential main amplifier and output stage. The balancing error integrator closes a feedback loop which removes the dc-offset between both output terminals by adjusting the dc-voltage at the inverting input of the main amplifier.

The transimpedance gain of the input stage and voltage gain of the main amplifier and output stage can be digitally modified using the built-in controller, in order to keep the output signal swing and associated linearity at a reasonable level for varying optical input powers. This approach yields a number of discrete gain modes, rather than a continuous range of supported gains, as offered by conventional analog gain control. For a given optical input power, the gain of each stage should be appropriately selected in order to minimize the penalty due to nonlinearity. Moreover, changing the transimpedance gain of the input stage modifies its dynamics, which is counteracted by means of an additional control element, as to be explained later on. Clearly, controlling these elements in a purely analog fashion is an arduous task, given the intricate relation between the circuit elements. The selected approach, however, employs digital control and incorporates a look-up table such that the gain and dynamics of each stage can be shaped to obtain the desired response [18]. The disadvantage of the employed discrete control is that, by its very nature, it cannot adjust the control elements by an infinitesimal amount. As such, a fixed output swing cannot be maintained for a varying input powers. Rather, the output swing can be kept within a finite range, dictated by the resolution of the control elements. Furthermore, the jump in the TIA output signal when switching occurs might cause a temporary disturbance to a clock-and-data recovery circuit after the TIA. Thus, gain control is to occur when the BER is not critical (e.g., during initialization, during a preamble), after which the input power is assumed to be relatively constant.

The TIA runs off a 2.5 V supply and draws 157 mW to 180 mW, depending on the selected input stage bias current. A die, containing two identical TIAs, was manufactured in a 0.13 µm SiGe BiCMOS process and is shown in Fig. 5(b). Each TIA occupies 1500 µm × 890 µm and was wirebonded to a PIN photodiode [19] with a responsivity of $\mathcal{R} = 0.6$ A/W.

### A. Transimpedance Input Stage

Fig. 6(a) shows a simplified small-signal equivalent circuit of a typical shunt-feedback TIA input stage [20] with a dc transimpedance gain of approximately $R_F$. On one hand, $R_F$ should be sufficiently large in order to reduce the contributions to the input-referred noise $i_\mathrm{n}^\mathrm{rms}$, originating from both $R_F$ itself and subsequent stages; on the other hand, $R_F$ should not be too large, taking into account the limited output voltage swing of the input stage. Hence, $R_F$ should be adjustable, such that it can be set according to the OMA.

We have opted to implement $R_F$ as the parallel connection of 32 n-channel metal-oxide semiconductor (nMOS) transistors, biased in the linear region. As such, $R_F$ can be controlled digitally by selectively enabling individual transistors: $R_F \approx 800\,\Omega/N$ with $N = 1, \ldots, 32$.

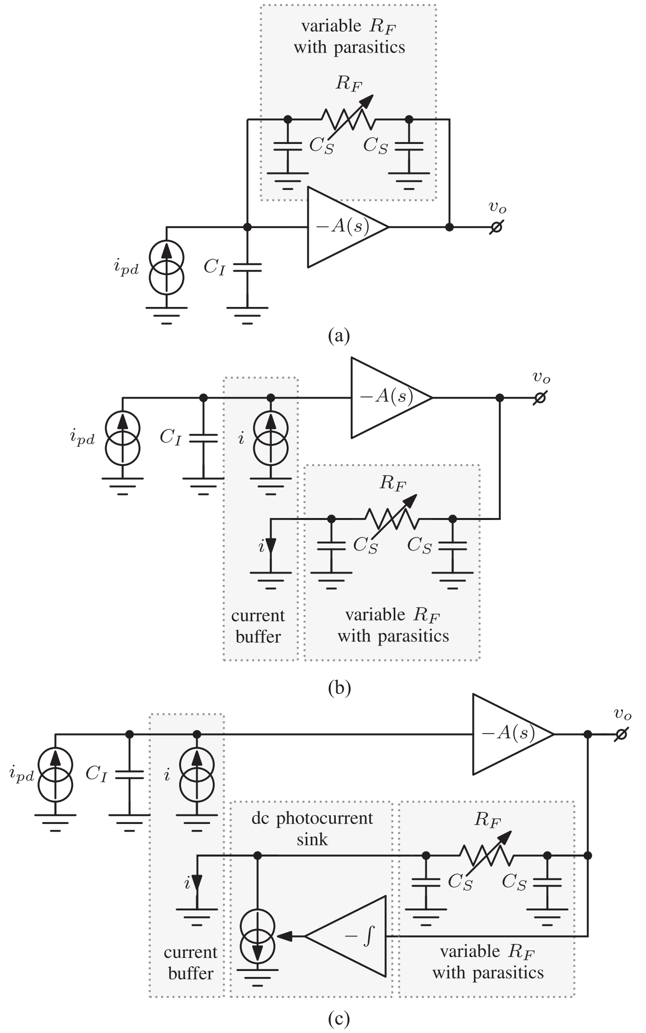

(a)

(b)

(c)

Fig. 6. Simplified small-signal equivalent circuit of (a) a shunt-feedback TIA and (b) an active-feedback TIA and (c) an active-feedback TIA with dc photocurrent sink.

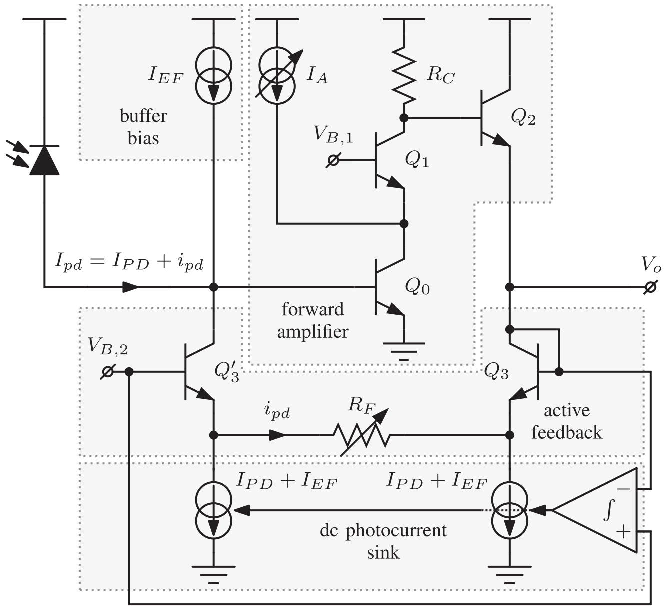

Fig. 7. Schematic of the active-feedback transimpedance input stage.

TABLE I
COMPONENT VALUES OF THE ACTIVE-FEEDBACK TRANSIMPEDANCE INPUT STAGE

| **component** | **value** |
|---|---|
| $Q_0$ | 40 µm |
| $Q_1$, $Q_2$, $Q_2'$, $Q_3$ | 12 µm |
| $R_C$ | 50 Ω |
| $R_F$ | 25 Ω–800 Ω |
| $I_{EF}$ | 3.2 mA |
| $I_A$ | 0 mA–9.6 mA |
| $V_{B,1}$ | 2.2 V |
| $V_{B,2}$ | 1.4 V |

This implementation, however, leads to significant parasitic capacitances $C_S$ on both sides of $R_F$. As illustrated in Fig. 6(a), this will increase the capacitance at the critical input node to $C_I + C_S$, which will impact the bandwidth. However, by placing a current buffer between feedback resistor $R_F$ and the input node, as shown in Fig. 6(b), $C_S$ no longer loads the input node. Moreover, it is effectively shorted by the low input impedance of the current buffer, nullifying its effect. The resulting topology is called an *active-feedback* TIA [20].

Considering the limited output voltage swing of the forward amplifier, the quiescent output voltage should be judiciously selected, independent of dc photocurrent, in order to maximize the output voltage swing. This is accomplished by modifying the circuit according to Fig. 6(c), an integrating loop sets to zero the contribution of the dc photocurrent to $v_o$. This loop is dimensioned such that the signal frequencies are not affected; for these frequencies Fig. 6(c) simply reduces to Fig. 6(b).

Assuming that $A(s) = A_0/(1 + s\tau)$, it follows from Fig. 6(b) that the transimpedance gain $Z_T(s)$ for the signal frequencies is given by

$$Z_T(s) = R_F \cdot \frac{1}{1 + s/(\omega_0 Q) + s^2/{\omega_0}^2} \tag{5}$$

with

$$\omega_0^2 = \frac{A_0}{R_F C_I \cdot \tau} \tag{6}$$

$$Q = \sqrt{\frac{A_0 \cdot \tau}{R_F C_I}}\,. \tag{7}$$

The parameters $\omega_0$ and $Q$ should be selected in order to limit the amount of ISI and noise. In order to maintain fixed values of $\omega_0$ and $Q$ for changing $R_F$, we adjust $A_0$ proportional to $R_F$.

Fig. 7 shows the schematic of the active-feedback transimpedance input stage. The corresponding component values are annotated in Table I, which also shows the emitter length for each BJT. The emitter width equals 0.27 µm for each BJT. The forward amplifier consists of a cascoded common-emitter amplifier formed by $Q_0$, $Q_1$ and $R_C$, followed by emitter follower $Q_2$; its gain $A_0$ is controlled by means of the adjustable dc current source $I_A$. The active feedback path is formed by diode-connected $Q_3$, $R_F$ and cascode $Q_3'$; the latter constitutes

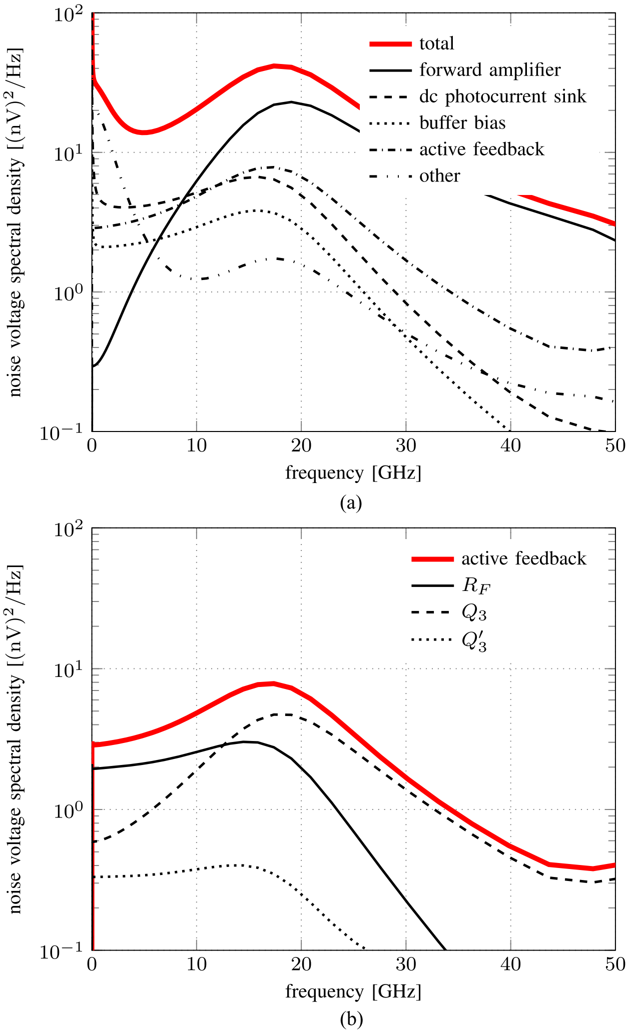

Fig. 8. Simulated noise spectral density at the output of the input stage, showing an overview of noise contributions due to several subcircuits (a) and a detail of noise contributions due to the active feedback subcircuit (b), both with $R_F = 160\,\Omega$ and $I_A = 9.2$ mA.

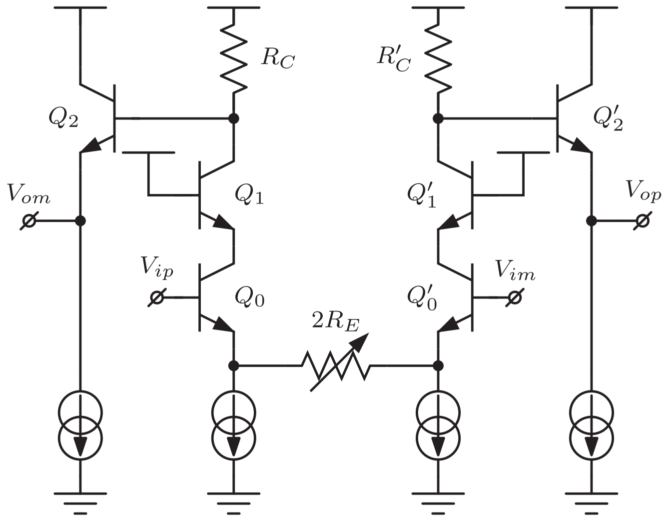

Fig. 9. Schematic of differential gain stage.

TABLE II
COMPONENT VALUES OF THE DIFFERENTIAL GAIN STAGES AND OUTPUT STAGE

| | **stage 1** | **stage 2** | **stage 3** | **output stage** |
|---|---|---|---|---|
| $Q_0$, $Q'_0$ | 3.6 µm | 5.4 µm | 7.2 µm | 14.4 µm |
| $Q_1$, $Q'_1$ | 1.2 µm | 1.8 µm | 2.4 µm | 7.2 µm |
| $Q_2$, $Q'_2$ | 2.4 µm | 3.6 µm | 4.8 µm | |
| $R_C$, $R'_C$ | 75 Ω | 50 Ω | 38 Ω | 50 Ω |
| $R_E$ | 4 Ω–72 Ω | 3 Ω–48 Ω | 2 Ω–36 Ω | 1 Ω–18 Ω |
| $I_1$, $I'_1$ | 1.6 mA | 2.4 mA | 3.2 mA | 6.4 mA |
| $I_2$, $I'_2$ | 0.8 mA | 1.2 mA | 1.6 mA | |

the current buffer from Fig. 6(b). The integrator controls both tail current sources such that the dc component of $V_o$ equals dc bias voltage $V_{B,2}$; as a result no dc current flows through $R_F$. The dc current source $I_{EF}$ ensures proper biasing of the input stage for a wide range of photocurrents.

Fig. 8(a) shows the simulated noise spectral density at the output $V_o$ of the input stage, revealing the contributions of each of the subcircuits annotated in Fig. 7. These simulation results were obtained with variable feedback resistor $R_F$ set to 160 Ω and dc current source $I_A = 9.2$ mA. Note that the vast majority of the noise is generated in the forward amplifier; its noise contribution is dominated by common-emitter BJT $Q_0$. Using a similar reasoning as in [17], we have selected a suitable biasing and sizing for $Q_0$, minimizing the noise contribution without compromising the dynamic behavior and linearity. Note from Table I that this results in a fairly large emitter area for $Q_0$; this is done to reduce the base resistance and the noise voltage it produces. While the noise contribution of the active feedback subcircuit is less prominent, it is shown that a significant portion of this contribution is generated by current buffer $Q_3$, as illustrated in Fig. 8(b).

### B. Main Amplifier and Output Stage

The main amplifier consists of three fully differential gain stages. The topology of such a gain stage is discussed at length in [17] and is illustrated in Fig. 9. The gain is controlled by adjusting degeneration resistor $2R_E$, which again is implemented as an nMOS transistor array, biased in the linear region. The output stage has a structure similar to the gain stage from Fig. 9, but without emitter followers $Q_2$ and $Q'_2$, and has $R_C = R'_C = 50\,\Omega$. The corresponding component values for each stage are annotated in Table II, which also shows the emitter length for each bipolar junction transistor (BJT). The emitter width equals 0.27 µm for each BJT.

### C. TIA Gain Modes

The TIA's built-in controller allows selecting between four transimpedance gain modes. These modes are characterized by the settings indicated in Table III. Going from mode 1 to 4, the total transimpedance gain is gradually reduced using both the input stage feedback resistor $R_F$ and the combined gain $A_{\text{post}}$ of the main amplifier and output stage. As such, the input-referred rms noise will gradually increase from mode 1 to 4, while the TIA's linearity will gradually increase. Note that $I_A$ is varied along with $R_F$ as explained in Section III-A.

TABLE III
TIA SETTINGS FOR GAIN MODES 1—4

| | | **mode 1** | **mode 2** | **mode 3** | **mode 4** |
|---|---|---|---|---|---|
| $R_F$ | Ω | 160 | 160 | 100 | 100 |
| $I_A$ | mA | 9.2 | 9.2 | 0 | 0 |
| $(R_E)_{\text{stage 1}}$ | Ω | 12 | 18 | 18 | 24 |
| $(R_E)_{\text{stage 2}}$ | Ω | 8 | 12 | 12 | 16 |
| $(R_E)_{\text{stage 3}}$ | Ω | 6 | 9 | 9 | 12 |
| $(R_E)_{\text{output stage}}$ | Ω | 3 | 4 | 4 | 6 |

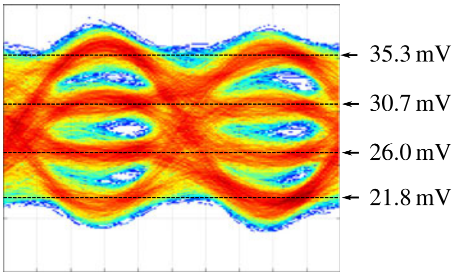

Fig. 10. 64 Gb/s PAM-4 transmitter eye diagram, measured using a high-bandwidth photodiode, with symbol levels annotated. Horizontal and vertical scale is 6.25 ps/div and 5 mV/div.

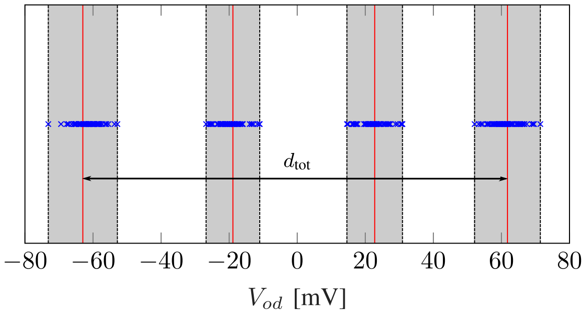

Fig. 11. Scatter diagram of the signal component, with gain mode 1 and −10.3 dBm OMA. ISI bands are annotated, along with $d_{\text{tot}}$.

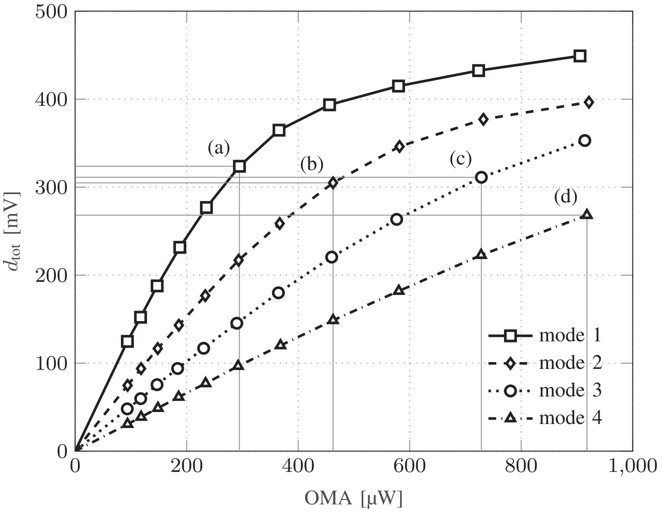

Fig. 12. Measured differential output voltage $d_{\text{tot}}$ as a function of OMA for gain modes 1—4. Operating points corresponding to eye diagrams Fig. 14(a) to (d) annotated as (a)—(d).

## IV. EXPERIMENTAL SETUP

The transmitter hardware consists of a continuous-wave 1550 nm laser and a $\geq 25$ GHz MZM, modulated by an electrical 64 Gb/s PAM-4 signal. This signal is the result of Gray-mapping a $2^9 - 1$ and is generated using a 64 GSa/s arbitrary waveform generator. The resulting transmitter eye diagram, as captured using a broadband photodiode directly connected to a 63 GHz oscilloscope, is shown in Fig. 10. Note that, due to the low conversion gain of the directly-connected photodiode, the signal swing is so small that the eye diagram is deteriorated due to noise from the oscilloscope itself. It was verified that the transmitter contribution to the noise and ISI at the output of the TIA is negligible compared to that of the TIA itself, such that the assumptions from Section II are met. In order to avoid compression due to the non-linear characteristics of the MZM [21], the drive voltage swing was limited, yielding a 2.1 dB extinction ratio, i.e., the ratio between the optical powers corresponding to the input levels $+A$ and $-A$ from (1b), as indicated on Fig. 10. At the receiving end, the optical signal is coupled into the photo diode by means of a manually aligned lensed fiber. The differential TIA output voltage is then captured at 160 GSa/s using a 63 GHz real-time oscilloscope for the duration of approximately $500 \times 10^3$ symbol periods. The above procedure was repeated for varying optical input powers and four transimpedance gain modes, selected using the TIA's built-in controller.

Based on the captured waveforms, a number of parameters and performance indicators were determined offline. Lowpass interpolation (i.e., the insertion of zeros between the original samples and subsequent lowpass filtering) was employed to increase the sample rate of these waveforms by a factor of 32 and 8 for eye diagram generation and BER calculation, respectively. For the latter, the appropriate decision instants and decision thresholds were determined, yielding the samples $v_k = v(kT + \epsilon)$, after which (i) the BER was obtained after symbol-by-symbol detection and error counting; (ii) the signal and noise contributions at the decision instants were separated, exploiting the periodicity of the signal component; (iii) the rms value $v_{\text{n}}^{\text{rms}}$ of the output noise voltage was computed; (iv) the useful and ISI contributions were identified from the scatter diagram of the signal component. Note that, in order to accurately portray the performance of the TIA itself, no pre-emphasis or post-equalizer was used, as these would correct the TIA's frequency response and reduce intersymbol interference.

## V. RESULTS AND DISCUSSION

Fig. 11 shows the scatter diagram of the signal component of the TIA differential output voltage, extracted from a measurement corresponding to gain mode 1 and −10.3 dBm OMA. The four ISI bands mentioned in Section II-A are easily discerned; the distance $d_{\text{tot}}$ between the centers of the outer ISI bands is indicated on the figure.

We have determined the distance $d_{\text{tot}}$ for various OMAs for each of the four gain modes. The result is shown in Fig. 12. As expected, the larger the total transimpedance gain, the smaller the input-referred linear range. For each gain mode, we have selected an operating point in the linear range and determined

TABLE IV
EXTRACTED TIA PARAMETERS FOR GAIN MODES 1—4

| | | **mode 1** | **mode 2** | **mode 3** | **mode 4** |
|---|---|---|---|---|---|
| $h_0$ | dB Ω | 67 | 62 | 59 | 55 |
| $\kappa$ | · | 0.144 | 0.153 | 0.138 | 0.143 |
| $\eta \cdot i_{\mathrm{n}}^{\mathrm{rms}}$ | µA | 4.9 | 5.9 | 7.9 | 10.2 |

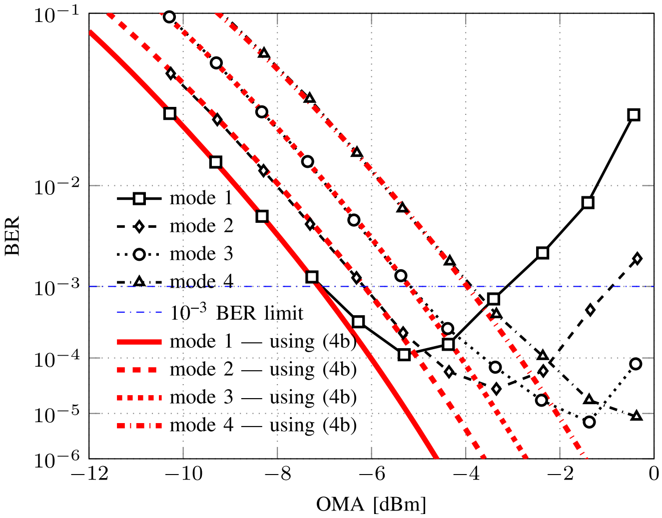

Fig. 13. Measured BER versus OMA for 64 Gb/s PAM-4, and calculated BER (4b) using a simplified model versus OMA.

the corresponding scatter diagram, from which we extracted the transimpedance impulse response coefficient $h_0$ and relative peak ISI magnitude $\kappa$, defined in Section II-A. From the rms value $v_{\mathrm{n}}^{\mathrm{rms}}$ of the output noise voltage and coefficient $h_0$, we computed $\eta \cdot i_{\mathrm{n}}^{\mathrm{rms}}$. These quantities are displayed in Table IV. Going from mode 1 to mode 4, $h_0$ decreases and $i_{\mathrm{n}}^{\mathrm{rms}}$ increases. The decrease of $h_0$ is consistent with the decreasing total gain indicated in Table III. The increase of $i_{\mathrm{n}}^{\mathrm{rms}}$ has the following causes: (i) reducing the (transimpedance) gain of each stage increases the input-referred noise contributions from subsequent stages [20]; (ii) reducing $R_F$ increases its input-referred noise contribution. As the current $I_A$ is varied along with feedback resistor $R_F$, the dynamics of the TIA are essentially independent of the gain mode; consequently, the corresponding relative peak ISI magnitude $\kappa$ remains fairly constant. With $\kappa \approx 0.15$ for all gain modes, the associated power penalties as a function of the operating BER are readily found in Fig. 3.

Fig. 13 shows the measured BER as a function of OMA for the considered gain modes. For a given gain mode, two regions can be identified, corresponding to small OMA (linear TIA operation) and large OMA (nonlinear TIA operation). For increasing OMA, the BER in the former and latter region is decreasing and increasing, respectively, confirming the analysis from Section II. Hence, for a given gain mode, a range $(\mathrm{OMA}_{\mathrm{low}}, \mathrm{OMA}_{\mathrm{high}})$ can be identified for which the BER does not exceed the BER limit[1] of $10^{-3}$. Going from mode 1 to 4, both $\mathrm{OMA}_{\mathrm{low}}$ and $\mathrm{OMA}_{\mathrm{high}}$ get larger; this behavior follows from the increase of the noise level ($\mathrm{OMA}_{\mathrm{low}}$), indicated in Table IV, and of the input-referred linear range ($\mathrm{OMA}_{\mathrm{high}}$), illustrated in Fig. 12. By selecting at each operating point the appropriate gain mode, the BER limit is achieved when the OMA is between −7 dBm and (at least) −0.2 dBm.

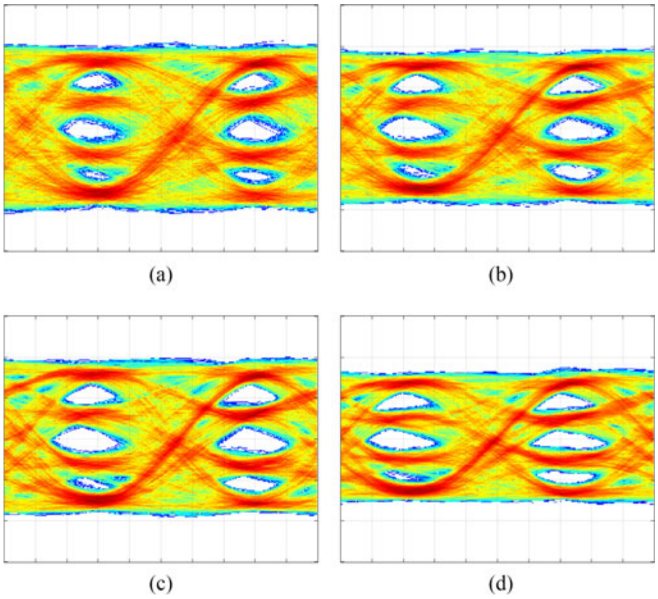
(a)
(b)
(c)
(d)

Fig. 14. Measured 64 Gb/s PAM-4 eye diagrams corresponding to the operating point yielding minimum BER. Horizontal and vertical scale is 6.25 ps/div and 100 mV/div for all eye diagrams. (a) mode 1, OMA = −5.2 dBm (b) mode 2, OMA = −3.3 dBm (c) mode 3, OMA = −1.3 dBm (d) mode 4, OMA = −0.2 dBm

Using the extracted TIA parameters from Table IV, the BER can be calculated according to (4b), which uses a simplified model as discussed in Section II-A. Fig. 13 compares the calculated BER (4b) with the measured BER for gain modes 1–4. Clearly, (4b) constitutes an excellent approximation of the measured BER in the linear region.

For each gain mode, Fig. 14 displays the eye diagram corresponding to the operating point yielding the smallest BER, qualitatively illustrating the satisfactory error performance with PAM-4 at 64 Gb/s. Note that the operating points corresponding to each eye diagram is annotated in Fig. 12.

Compared to the 64 Gb/s results from our previous contributions, gain switching significantly improves [13] in terms of dynamic range and OMA sensitivity (from 0 dBm to −7 dBm), and the redesigned input stage enhances the sensitivity from [14] by 1 dB. These advantages come with only a slight increase in power consumption of 15 mW and 30 mW, compared to [13] and [14], respectively. Other state-of-the-art publications detailing PAM-4 BER measurements at similar bit rates report a higher TIA power consumption [9], [22] or mention no power consumption at all [10]. Real-time 60 Gb/s BER measurements are presented in [22], achieving BER=$10^{-3}$ sensitivity at an average optical input power of −1.3 dBm using a commercial TIA that consumes 1200 mW. Complex experiments are presented in [7]–[10], for which the TIA plays only a minor role; their BER results are achieved using power-hungry digital

---

[1] We assume that a raw BER of $10^{-3}$ is sufficiently small for the FEC in the eventual application to achieve a suitable system BER.

signal processing techniques involving FFE and DFE. Furthermore, one of [9]'s results is achieved using an avalanche photodiode, whereas [10] used an Erbium-doped optical fiber amplifier with 25 dB gain in front of the photodiode to significantly boost the received input power.

## VI. CONCLUSION

We have presented a TIA for 64 Gb/s PAM-4 optical links, implemented in 0.13 μm SiGe BiCMOS with a power consumption of 180 mW. During the design of the TIA, we have taken into account the challenges related to the use of PAM-4, i.e., increased susceptibility to noise, ISI, and receiver nonlinearity. A digital gain controller enables the switching between four discrete gain modes, thereby allowing a trade-off between sensitivity and linearity. Furthermore, the transimpedance gain of the input stage can be varied with little effect on the relative ISI magnitude. Compared to our previous contributions, we were able to improve the dynamic range of [13] and the sensitivity of [13], [14], due to the inclusion of gain control, as well as the redesigned input stage. The TIA performance was experimentally validated using BER measurements. The raw BER limit of $10^{-3}$ is achieved for OMAs between $-7$ dBm and at least $-0.2$ dBm. Moreover, TIA parameters were extracted from the measurements and fed into a simplified model, the results of which closely match the measured BER in the linear region.

## ACKNOWLEDGMENT

The authors would like to thank Albis Optoelectronics AG for providing the photodiodes used in this work, and A. Sandomirsky, who is with Mellanox Technologies, Israel.

## REFERENCES

[1] "IEEE P802.3bs baseline summary." [Online]. Available: http://www.ieee802.org/3/bs/baseline_3bs_0715.pdf. Accessed on: Jan. 3, 2015.

[2] F. Karinou, N. Stojanovic, and C. Prodaniuc, "56 Gb/s 20-km transmission of PAM-4 signal employing an EML compensation in C-band without in-line chromatic dispersion compensation," in *Proc. Eur. Conf. Opt. Commun.*, 2016, pp. 1–3.

[3] P. P. Baveja *et al.*, "56 Gb/s PAM-4 directly modulated laser for 200 G/400 G data-center optical links," in *Proc. Opt. Fiber Commun. Conf.*, 2017, pp. 1–3.

[4] M. Kim, S. H. Bae, H. Kim, and Y. C. Chung, "Transmission of 56-Gb/s PAM-4 signal over 20 km of SSMF using a 1.55-μm directly-modulated laser," in *Proc. Opt. Fiber. Commun. Conf.*, 2017, pp. 1–3.

[5] W. Soenen, R. Vaernewyck, X. Yin, S. Spiga, and M.-C. Amann, "56 Gb/s PAM-4 driver IC for long-wavelength VCSEL transmitters," in *Proc. Eur. Conf. Opt. Commun.*, 2016, pp. 1–3.

[6] S. Moazeni *et al.*, "A 40 Gb/s PAM-4 transmitter based on a ring-resonator optical DAC in 45 nm SOI CMOS," in *Proc. Int. Solid-State Circuits Conf.*, 2017, vol. 60, pp. 486–487. [Online]. Available: http://ieeexplore.ieee.org/document/7870473/

[7] N. Eiselt *et al.*, "Evaluation of real-time 8 × 56.25 Gb/s (400 G) PAM-4 for inter-data center application over 80 km of SSMF at 1550 nm," *J. Lightw. Technol.*, vol. 35, no. 4, pp. 955–962, Feb. 2017. [Online]. Available: http://ieeexplore.ieee.org/document/7589089/

[8] N. Eiselt *et al.*, "Experimental demonstration of 56 Gbit/s PAM-4 over 15 km and 84 Gbit/s PAM-4 over 1 km SSMF at 1525 nm using a 25 G VCSEL," in *Proc. 42nd Eur. Conf. Opt. Commun.*, 2016, pp. 1–3.

[9] Y. F. Chang, "Link performance investigation of industry first 100 G PAM4 IC chipset with real-time DSP for data center connectivity," in *Proc. Opt. Fiber Commun. Conf.*, 2016, Paper Th1G.2. [Online]. Available: http://www.osapublishing.org/abstract.cfm?uri=OFC-2016-Th1G.2

[10] J. Wei *et al.*, "Demonstration of the first real-time end-to-end 40-Gb/s PAM-4 for next-generation access applications using 10-Gb/s transmitter," *J. Lightw. Technol.*, vol. 34, no. 7, pp. 1628–1635, Apr. 2016. [Online]. Available: http://ieeexplore.ieee.org/lpdocs/epic03/wrapper.htm?arnumber=7384416

[11] N. A. Quadir, P. D. Townsend, and P. Ossieur, "An inductorless linear optical receiver for 20 Gbaud/s (40 Gb/s) PAM-4 modulation using 28 nm CMOS," in *Proc. IEEE Int. Symp. Circuits Syst.*, 2014, pp. 2473–2476. [Online]. Available: http://ieeexplore.ieee.org/lpdocs/epic03/wrapper.htm?arnumber=6865674

[12] K. Yu *et al.*, "56 Gb/s PAM-4 optical receiver frontend in an advanced FinFET process," in *Proc. IEEE 58th Int. Midwest Symp. Circuits Syst.*, 2015, pp. 1–4.

[13] B. Moeneclaey *et al.*, "A 64 Gb/s PAM-4 linear optical receiver," in *Proc. Opt. Fiber Commun. Conf.*, 2015, Paper M3C.5. [Online]. Available: https://www.osapublishing.org/abstract.cfm?uri=OFC-2015-M3C.5

[14] B. Moeneclaey, J. Verbrugghe, E. Mentovich, P. Bakopoulos, J. Bauwelinck, and X. Yin, "A 64 Gb/s PAM-4 transimpedance amplifier in 0.13 μm SiGe BiCMOS," in *Proc. 21st Annu. Symp. IEEE Photon. Benelux*, 2016, pp. 259–262.

[15] B. Moeneclaey, J. Verbrugghe, E. Mentovich, P. Bakopoulos, J. Bauwelinck, and X. Yin, "A 64 Gb/s PAM-4 transimpedance amplifier for optical links," in *Proc. Opt. Fiber Commun. Conf.*, 2017, pp. 1–3.

[16] J. G. Proakis, *Digital Communications*, 4th ed. New York, NY, USA: McGraw-Hill.

[17] B. Moeneclaey *et al.*, "A 40-Gb/s transimpedance amplifier for optical links," *IEEE Photon. Technol. Lett.*, vol. 27, no. 13, pp. 1375–1378, Jul. 2015. [Online]. Available: http://ieeexplore.ieee.org/lpdocs/epic03/wrapper.htm?arnumber=7083748

[18] J. Verbrugghe, "Design of event-driven automatic gain control and high-speed data path for multichannel optical receiver arrays," Ph.D. dissertation, Faculty of Eng. and Architect., Ghent University, Ghent, Belgium, 2015.

[19] Albis Optoelectronics AG, "PDCS12T 43 Gb/s photodiode." [Online]. Available: http://www.albisopto.com/albis_product/pdcs12t/. Accessed on: Jul. 1, 2017.

[20] E. Säckinger, *Broadband Circuits for Optical Fiber Communication*. Hoboken, NJ, USA: Wiley. [Online]. Available: http://doi.wiley.com/10.1002/0471726400

[21] P. Winzer and R.-J. Essiambre, "Advanced optical modulation formats," *Proc. IEEE*, vol. 94, no. 5, pp. 952–985, May 2006.

[22] P. Westbergh, M. Karlsson, A. Larsson, P. Andrekson, and K. Szczerba, "60 Gbits error-free 4-PAM operation with 850 nm VCSEL," *Electron. Lett.*, vol. 49, no. 15, pp. 953–955, Jul. 2013. [Online]. Available: http://digital-library.theiet.org/content/journals/10.1049/el.2013.1755

**Bart Moeneclaey** (M'14) was born in Ghent, Belgium, in 1988. He received the Engineering degree in applied electronics from Ghent University, Ghent, Belgium, in 2011, where he is currently working toward the Ph.D. degree. Since 2011, he has been a Research Assistant in the IDLab Design group, Ghent University. His research is focused on amplifier circuit design for high-speed optical communication systems.

**Jochen Verbrugghe** received the M.S. degree in computer science engineering and the M.S. degree in electrical engineering from Ghent University, Belgium, in 2007 and 2009, respectively. In 2014, at the the IDLab Design group of Ghent University, he obtained the Ph.D. degree, working on high speed optical receivers. He is now with Broadcom Ltd.

**Joris Lambrecht** was born in Ghent, Belgium, in 1992. He received the M.S. Degree in electrical engineering from Ghent University, Ghent, Belgium, in 2015, where he is currently working toward the Ph.D. degree. Since 2015, he has been a Research Assistant in the IDLab Design group, Ghent University. His research focusses on high-speed optical receiver design.

**Elad Mentovich**, biography not available at the time of publication.

**Paraskevas Bakopoulos**, biography not available at the time of publication.

**Johan Bauwelinck** (M'02) received the Ph.D. degree in applied sciences, electronics from Ghent University, Ghent, Belgium, in 2005. Since October 2009, he has been a Professor in the INTEC Department at the same university, and since 2014, he has been leading the IDLab Design group. He was and is active in the EU-funded projects GIANT, POWERNET, PIEMAN, EuroFOS, C3-PO, Mirage, Phoxtrot, Spirit, Flex5Gware, Teraboard, Streams, and WIPE conducting research on advanced electronic integrated circuits for next generation transport, metro, access, datacenter, and radio-over-fiber networks. He has promoted 18 Ph.Ds. and coauthored more than 150 publications and 10 patents in the field of high-speed electronics and fiber-optic communication. His research interests include high-speed, high-frequency (opto-) electronic circuits and systems, and their applications on chip and board level, including transmitter and receiver analog front-ends for wireless, wired and fiber-optic communication or instrumentation systems.

**Xin Yin** (M'06) received the B.E. and M.Sc. degrees in electronics engineering from the Fudan University, Shanghai, China, in 1999 and 2002, respectively, and the Ph.D. degree in applied sciences, electronics from Ghent University, Ghent, Belgium, in 2009. Since 2007, he has been a staff Researcher in IMEC-INTEC, and since 2013, he has been a Professor in the INTEC Department at Ghent University. His current research interests include high-speed and high-sensitive optoelectronic circuits and subsystems, with emphasis on burst-mode receiver and CDR/EDC for optical access networks, and low-power mixed-signal integrated circuit design for telecommunication applications. He led a team that won the GreenTouch 1000x award together with Bell Labs/Alcatel-Lucent and Orange Labs in Nov. 2014 and he is a member of the ECOC technical program committee.